ELSEVIER

Chemical Engineering Journal 141 (2008) 305–317

Chemical Engineering Journal

www.elsevier.com/locate/cej

ERT algorithms for quantitative concentration measurement of multiphase flows

R. Giguère[a], L. Fradette[a,*], D. Mignon[b], P.A. Tanguy[a]

[a] *Department of Chemical Engineering, URPEI, Ecole Polytechnique of Montreal, P.O. Box 6079, Montreal H3C 3A7, Canada*

[b] *Total Petrochemicals Research Feluy, Belgium*

Received 31 July 2007; received in revised form 2 January 2008; accepted 3 January 2008

Abstract

A quantitative image reconstruction algorithm for electrical resistance tomography (ERT) has been developed to visualize multiphase flows, like slurry flows in pipes. Based on image reconstruction techniques from literature, a generalized iterative algorithm (GIA) has been derived to solve the ERT inverse problem. Performance of this algorithm has been studied for synthetic and experimental test cases representing rods and solid particle beds in a pipe.

Quantitative images have been obtained for each test case and a suitable strategy for the image reconstruction has been identified. In particular, it was found that convergence of the GIA can be ensured using Landweber or Tikhonov iterations, an efficient forward problem solver and an appropriate relaxation factor. Finally, experimental calibration curve of concentration of solid particle beds in a horizontal pipe has been done using the GIA. Results show the capability of ERT to produce quantitative concentration measurements of multiphase flows.

Keywords: Tomography; ERT; Image reconstruction; Inverse problem; Multiphase flow

1. Introduction

Electrical resistance tomography (ERT) is a non-intrusive process tomography technique, aiming at visualizing multiphase flows. ERT systems are composed of a hardware part, which includes the sensor with electrode ring(s), the data acquisition system, and the computer to generate images. The working principle consists of injecting electrical current between a pair of electrodes and measuring the potential differences between the remaining electrode pairs. This procedure is repeated for all the other electrode pairs until a full rotation of the electrical field is completed to form a set of measurements. Each dataset is interpreted by image reconstruction algorithms to compute a cross-sectional image corresponding to the electrical conductivity inside the sensor. The concentration of each phase can be computed based on the knowledge of the electrical conductivity of each phase, yielding the concentration tomogram.

ERT can be applied to various processes involving a conductive fluid as the continuous phase. Typical applications of ERT are the visualization of multiphase flow in pipes and agitated tanks, for which commercial devices are now available for a wide range of sensor dimensions and materials. Examples of applications for electrical tomography have been reviewed [1–3] and recent applications for ERT are reported in Table 1.

The advantage of ERT lays in its excellent time resolution arising from the very fast measurements of electrical resistances. Moreover, electrical tomography techniques are safe and cheap in comparison to nuclear techniques, and make them suitable for both research and process industry. The drawback of ERT resides in the relatively low spatial resolution, reported as being between 3 and 10% of the sensor diameter [2,4]. In fact, electrical tomography is considered as a soft-field technique since the image is based on measurements at the periphery of the sensor and the image reconstruction involves resolution of a mathematically challenging inverse problem.

Over the years, many image reconstruction techniques have been proposed for electrical tomography, but the simplest one, the linear back-projection (LBP), is still the most widely used because it allows online imaging. The excellent time resolution

---

* Corresponding author. Tel.: +1 514 340 4040; fax: +1 514 340 4105.
E-mail address: louis.fradette@polymtl.ca (L. Fradette).

1385-8947/$ – see front matter © 2008 Elsevier B.V. All rights reserved.
doi:10.1016/j.cej.2008.01.011

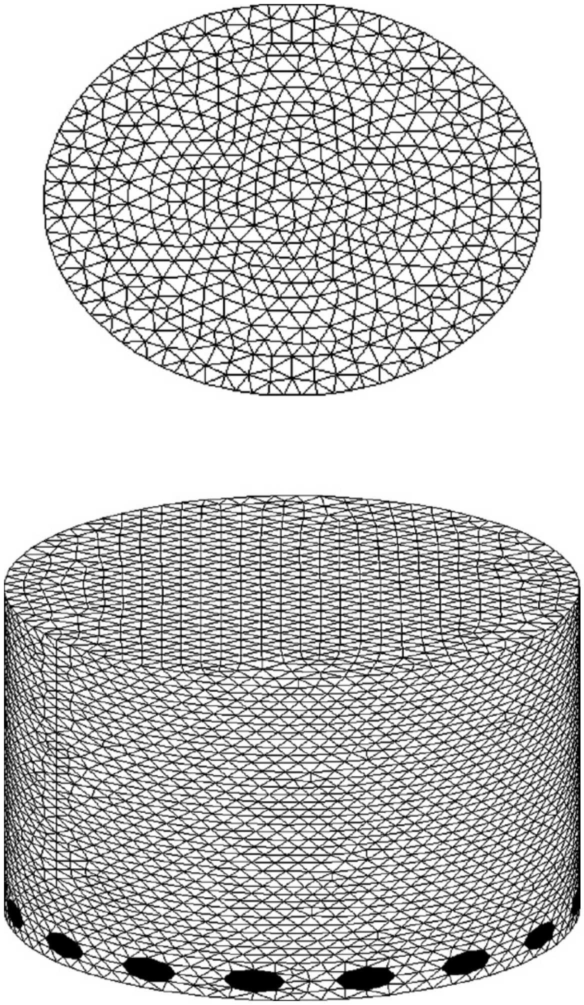

Fig. 1. Meshes of ERT sensor used to generate synthetic data and reconstruct image with GIA: (i) 2D mesh (1028 P1 finite elements, 563 nodes) and (ii) 3D mesh (78,898 P1 finite elements, 15,298 nodes).

and the qualitative images provided by LBP are often sufficient to monitor and visualize transient multiphase flows.

Quantitative tomography techniques are important to characterise a multiphase flow and efficient strategies of image reconstruction for ERT must be developed. Despite the numerous efforts on image reconstruction deployed in electrical tomography, there are very few reports concerning the performance, validation, and limitations of quantitative image reconstruction techniques [5,6]. The selection of the most suitable image reconstruction strategy to support the adequate interpretation of ERT images is often hampered by the lack of experimentally validated results.

Most of the efforts made in electrical tomography for the development of image reconstruction techniques and their quantitative validation were made in electrical capacitance tomography (ECT). Among the works on ECT offering a confrontation with synthetic and experimental data, investigations in [7–11] have compared results for various image reconstruction techniques for both synthetic and experimental data. In general, iterative methods have been reported to improve the precision of the results in comparison to direct methods, like the LBP.

Table 1
Recent applications of ERT to monitor multiphase flow

Applications	Phases	References
Pipe flow	S–L	[18–21]
	G–L	[22–24]
	L–L	[25,26]
Agitated tank	L–L	[27,28]
	G–L	[27]
	S–L	[29]
Packed-bed reactor	S–L	[30]
Bubble column	G–L	[31–35]

Despite the effectiveness of the iterative methods to provide quantitative results when used in very controlled environments, the selection of the appropriate algorithm and related numerical parameters often requires a trial-and-error scheme to reach a solution comparable to the experiments. It can obviously be envisaged to transpose the image reconstruction techniques used for ECT to ERT since there is a simple mathematical analogy between them, but the performance of these algorithms must systematically be evaluated and an efficient strategy must be devised to free the algorithms from the dependence on manual selection of parameters.

The present work aims at developing a quantitative image reconstruction method usable for ERT. First, a generalized iterative algorithm (GIA) is devised from the generalization of the image reconstruction techniques available in the electrical tomography literature. Then, the performance of two iterative image reconstruction techniques is investigated for synthetic data to identify a reliable strategy to reconstruct quantitative images from ERT. Finally, the performance of the proposed GIA is assessed by confrontation of the reconstructed images with experimental data. A parallel comparison of the results with the output from the commercial software using the LBP algorithm is also made.

2. Image reconstruction for ERT

2.1. Problem formulation

The goal of image reconstruction in ERT is to compute a tomogram representing the electrical conductivity of materials flowing within the sensor from voltages measured at the periphery of the sensor in response to the injected electrical current. The electrical conductivity σ and electrical potential Φ are governed by the Maxwell relations and simplifications in the case of ERT lead to the classical Poisson equation:

$$\nabla(\sigma\nabla\Phi) = 0 \quad \text{in } \Omega, \tag{1}$$

where Ω represents the domain occupied by the medium to analysis. Boundary conditions for Eq. (1) are given by

$$\sigma\frac{\partial\Phi}{\partial n} = c \quad \text{in } \partial\Omega, \tag{2}$$

where n is the vector normal to the sensor periphery $\partial\Omega$. The current density in Eq. (2) is given by

$$c = \begin{cases} I/A & \text{in } \partial\Omega_+ \\ -I/A & \text{in } \partial\Omega_- \\ 0 & \text{in } \partial\Omega\backslash(\partial\Omega_+ \cap \partial\Omega_-) \end{cases} \tag{3}$$

where $\partial\Omega_+$ and $\partial\Omega_-$ are the surfaces of the source and sink electrodes, respectively, A is the area of electrode and I is the electrical current. The potential drop at the fluid–electrode interface can be included in Eq. (2) leading to complete electrode model (CEM):

$$\Phi + z\sigma\frac{\partial\Phi}{\partial n} = V \quad \text{in } \partial\Omega_V, \tag{4}$$

where z is the electrode's contact impedance and V is the potential at the electrode surface $\partial\Omega_{\mathrm{V}}$.

2.2. Forward problem

Knowing the distribution of σ (i.e. the image), the problem of finding the electrical potential and potential differences V between electrode pairs for a given current injection is called the *forward problem* and it is denoted:

$$V = F(\sigma), \tag{5}$$

where F is defined as the forward operator governed by Eq. (1) with boundary conditions given by Eqs. (2), (3) and (4).

Finite element methods (FEM) are widely used to solve the forward problem in electrical tomography [6]. Nowadays, many FEM implementations are available for this well-known Poisson equation problem necessitating a simple inversion of a linear system. In the case of ERT, it provides an approximation of the potential differences for a given conductivity distribution σ, denoted:

$$V_{\mathrm{FEM}} = F_{\mathrm{FEM}}(\sigma), \tag{6}$$

where F_{FEM} is called the FEM forward operator. The conductivity distribution is generally defined as a constant per element in the mesh, each discrete value corresponding to a pixel of the image.

Another forward operator can be derived from the linearization of Eq. (5). The change in voltage differences $V + \Delta V$ in response to a perturbation of conductivity distribution $\sigma + \Delta\sigma$ can be expressed by the Taylor expansion:

$$\Delta V = \frac{\partial F}{\partial\sigma}(\Delta\sigma) + O((\Delta\sigma)^2). \tag{7}$$

Neglecting the higher order terms, Eq. (7) is simplified to the linear form:

$$\Delta V = s\,\Delta\sigma, \tag{8}$$

where $s = \partial F(\sigma)/\partial\sigma$ is the Jacobian matrix, also referred to in literature as the sensitivity matrix, which is computed based on multiple solutions of the FEM forward operator. Methods for the computation of the sensitivity matrix have been discussed in details in [6,12]. In their normalised form, the voltage, conductivity and sensitivity matrix are defined as

$$U_i = \frac{\Delta V_i}{V_i}, \tag{9}$$

$$G_j = \frac{\Delta\sigma_j}{\sigma_j}, \tag{10}$$

$$S_{ij} = \frac{s_{ij}}{\sum_{k=1}^{N} s_{ik}} \tag{11}$$

and Eq. (8) is rewritten to

$$U = \mathrm{SG}. \tag{12}$$

The linear forward projection operator is simply:

$$F_{\mathrm{S}} = \mathrm{SG}. \tag{13}$$

2.3. Inverse problem

Finding the conductivity distribution σ based on the voltages measurements V_{M} is called the *inverse problem* of ERT. Based on the previous notation, the inverse problem is to find the inverse of the forward operator:

$$\sigma = F^{-1}(V). \tag{14}$$

In its normalised linear form, the ERT inverse problem computes the inverse of the sensitivity matrix (12):

$$G = S^{-1}U. \tag{15}$$

In general, direct analytical solution for Eq. (14) or (15) does not exist since F is a non-linear operator with more unknown conductivity values than known voltage measurements. In that context, only approximations of F^{-1} or S^{-1} can be found by numerical techniques, representing both challenges and limitations for ERT imaging.

Approximations of S^{-1} are commonly derived using an optimisation method by computing a conductivity distribution, which minimises the difference between the measured voltages and the simulated voltages. With L_2-norm, that corresponds to solving the least-square minimisation problem:

$$\hat{G} = \underset{G}{\arg\min}||U_{\mathrm{M}} - F(G)||_2^2, \tag{16}$$

for which both direct and iterative algorithms can be formulated.

Many reviews about electrical tomography image reconstruction techniques are available in the literature (e.g. [6,7,13,14]). The choice of the approximation of S^{-1} in Eq. (15) leads to different image reconstruction algorithms summarized in Table 2. The simplest choice is to use the transpose of S, which corresponds to the linear back projection (LBP) and Landweber method. The Newton–Raphson method (NRM) appears to be very sensitive to the noise in the raw measurements because of ill-conditioned Hessian matrix [6,12]. Therefore, a modified Newton–Raphson method (MNRM), which includes a regularization property, is commonly preferred. Depending on the choice of regularization matrix, the Tikhonov method or the

Table 2
Approximations of S^{-1} in GIA

Algorithms	$\hat{S}^{-1}$
LBP/Landweber	S^{T}
Newton–Raphson	$(SS^{\mathrm{T}})^{-1}S^{\mathrm{T}}$
Tikhonov	$(SS^{\mathrm{T}}+\lambda I)^{-1}S^{\mathrm{T}}$
Levenburg–Marquardt	$(SS^{\mathrm{T}}+\lambda W)^{-1}$

Levenburg–Marquardt method can be obtained. In general, a large value of the regularization parameter λ tends to attenuate the presence of noise in data, but also reduces the precision of the reconstructed image [7]. Thus, the choice of the regularization parameter λ is seen as a compromise between the noise level and the desired precision of the solution.

Single-value decomposition (SVD) can be used to solve the inverse problem but it is very sensitive to the noise as well, even in presence of very small singular values. Truncated single-value decomposition (TSVD) can alleviate the problem by filtering the singular values. With the MNRM and TSVD methods, some regularization parameters must be fitted as a function of the noise level, mostly by a trial-and-error method. The preconditioned conjugate gradient method can also be used to solve the inverse problem of ERT.

3. A generalized image reconstruction algorithm for ERT

In this work, the reconstruction algorithms developed for ERT are synthesised in the following iterative form:

$$\begin{aligned}\hat{G}_{k+1} &= \hat{G}_k + \tau_k \hat{S}_k^{-1} R_k, \quad \text{for } (k = 1, 2, 3 \ldots)\\ R_k &= U_{\mathrm{M}} - F(\hat{G}_k),\end{aligned} \tag{17}$$

where $\hat{S}_k^{-1}$ is the approximation of the inverse of S_k at iteration k, τ_k is a relaxation parameter and R_k is the voltage residual to be minimised, which represents the difference between the measured voltages and the voltages computed by the forward projection operator F. The general form of Eq. (17) is called the generalized iterative algorithm (GIA) and the image reconstruction techniques in literature can be classified according to

- the choice of approximation of sensitivity matrix inverse $\hat{S}^{-1}$ (Table 2);
- the choice of forward operator F used in the calculation of the residuals R (F_{FEM} or F_{S});
- the update of the sensitivity matrix $S_k = S(\hat{G}_k)$ during the iterations;
- the choice of the relaxation parameter τ_k.

The filtering operator $P(G)$ defined in Eq. (18) can also be incorporated in Eq. (17) to make sure that iterations converge to a convex set, where conductivity is upper bounded (G_{U}) and lower bounded (G_{L}):

$$P(G) = \begin{cases} G_{\mathrm{L}} & \text{if } G < G_{\mathrm{L}} \\ G & \text{if } G_{\mathrm{L}} \le G \le G_{\mathrm{U}} \\ G_{\mathrm{U}} & \text{if } G_{\mathrm{U}} > G \end{cases}, \tag{18}$$

Finally, a stopping criterion is chosen such as the rate of change between reconstructed images (Eq. (19)) is less than a preset parameter ε:

$$\frac{||\hat{G}_{k-1} - \hat{G}_k||}{||\hat{G}_{k-1}||} \le \varepsilon. \tag{19}$$

3.1. Relaxation parameter

The relaxation parameter τ takes into account the nonlinearity of the inverse problem and control the convergence rate of the GIA. The simplest choice for τ is to use a relatively small constant value which ensures slow convergence of Eq. (17) at the price of a larger number of iterations. This value is usually determined by a trial-and-error method.

To alleviate the choice of an appropriate relaxation parameter, some authors have suggested strategies to re-evaluate τ each iteration. In the case of Landweber iteration, optimal step-length was derived by minimising the norm of the error residual R using an additional computation of the forward solution, at each iteration [15,16] namely

$$\tau = \frac{||S^{\mathrm{T}}R||_2^2}{||SS^{\mathrm{T}}R||_2^2}. \tag{20}$$

It is possible to extend the calculation of the optimal step-length for the case of GIA leading to a generalized pseudo-optimal relaxation parameter τ^*:

$$\tau_k^* = \frac{F(\hat{S}_k^{-1}R_k)^{\mathrm{T}} R_k}{||F(\hat{S}_k^{-1}R_k)||_2^2}. \tag{21}$$

The value for τ_k^* calculated by Eq. (21) depends both on the approximation of $\hat{S}_k^{-1}$ and the forward operator F used in the GIA. Linearity of the forward operator is assumed in the derivation of Eq. (21). This assumption is however not rigorously true. Therefore, an under-relaxation factor η can be necessary to ensure convergence:

$$\tau^{**} = \eta\tau^*. \tag{22}$$

Thus, the relaxation parameters defined by Eq. (21) or (22) are an alternative to the constant τ value and they can be used for any choice of $\hat{S}^{-1}$ and F in the GIA.

4. GIA experiments with synthetic images

A study was carried out to evaluate the performance of the GIA in ERT image reconstruction by using synthetic data from a set of known images. For each test case, synthetic voltage differences were computed using a sensor model

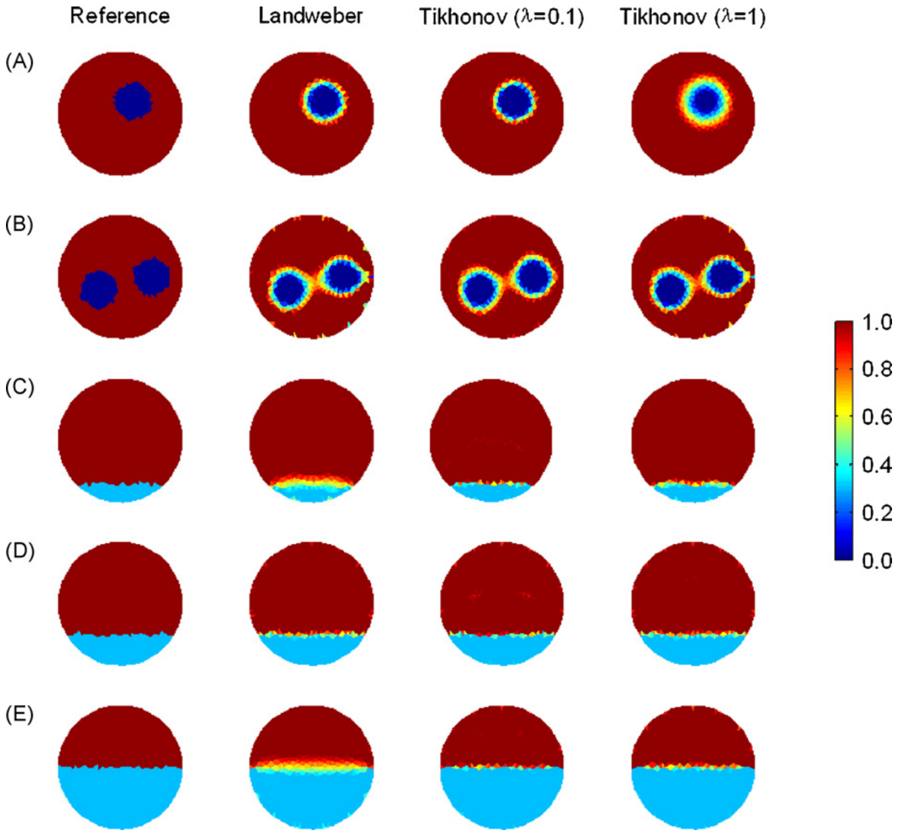

Fig. 2. Reconstructed images using GIA with ideal synthetic data ($\eta = 1$, $\varepsilon = 5 \times 10^{-7}$).

solving the forward problem of ERT for the corresponding conductivity distribution. Then, the synthetic data were used to reconstruct the image with our implementation of the GIA.

For that purposes, the geometry and dimensions of a commercial ERT sensor device (ITS, UK) was considered. It consists of a 3 in. pipe sensor having 16 circular electrodes of 8 mm in diameter mounted in a ring and using adjacent protocol of measurement. The meshes of the pipe sensor used in this work for the FEM sensor model are shown in Fig. 1.

A set of five test cases was used in these performance experiments: two cases represent non-conductive rods (referenced as A: one rod; B: two rods) at different location in the sensor; three cases represent different heights of solid particles forming a bed at the bottom of a pipe (referenced as C, D, and E, in increasing order). The conductivity of the continuous (most conductive) phase was assigned to 300 μS/cm for each test case, while the non-conductive rods were associated with a 1 μS/cm conductivity. In the case of the solid particle bed, the minimum value of the conductivity for a solid–liquid mixture was computed by the Maxwell equation:

$$\sigma = \frac{2 - 2C_s}{2 + C_s}\sigma_L, \tag{23}$$

where σ_L is the conductivity of the liquid conductive phase and C_s is the solid concentration of non-conductive solid particles. Considering the maximum packing limit of particles in the bed is about 0.6 for solid spheres, a value of $0.3\sigma_L$ was obtained for the electrical conductivity of the bed (90 μS/cm). Also, a current of 15 mA was injected with adjacent pair strategy for the protocol measurement.

For each test case studied in the following, the GIA was used to reconstruct the images using Landweber iterations and Tikhonov iterations with two different values for the regulariza-

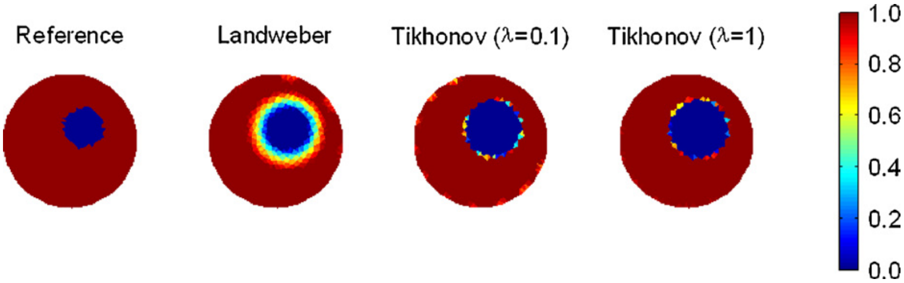

Fig. 3. Reconstructed images for the test case A with ideal synthetic data using linear forward projection ($\eta = 1$, $\varepsilon = 5 \times 10^{-7}$).

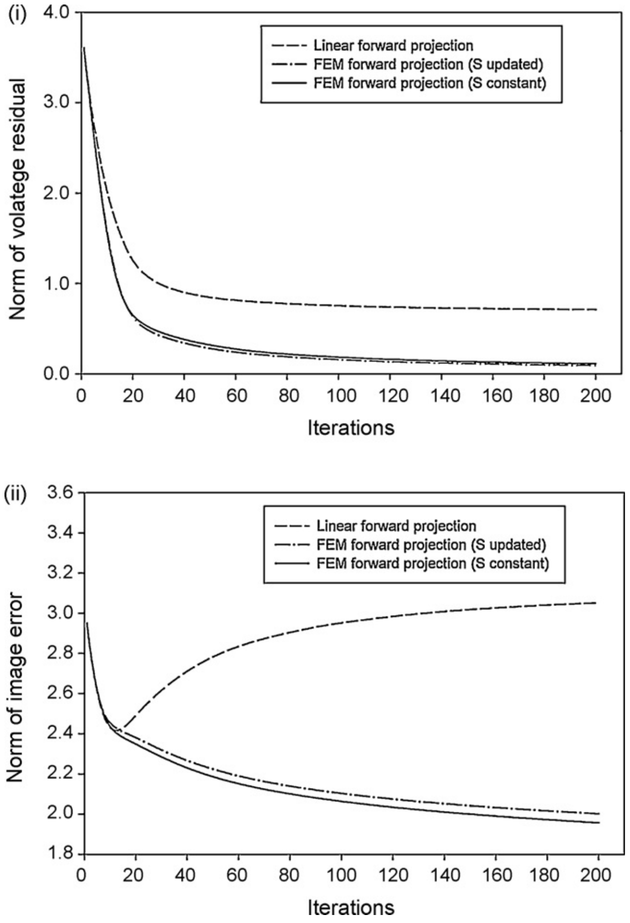

Fig. 4. Norm of voltage residual error (i) and conductivity error (ii) of images reconstructed for the test case A (Landweber iterations, $\tau = 0.1$).

tion parameters ($\lambda = 0.1$ and 1). Also, the 2D FEM sensor model (Fig. 1i) was used to solve the forward problem and compute the sensitivity matrix in GIA, given an image with 1028 unknown pixels. The upper and lower limits of conductivity on images were imposed in GIA using the projection operator defined in Eq. (18) ($G_U = 1.0$ for conductive phase, $G_L = 0.3$ for solid particle bed and $G_L = 0.0001$ for rods). A maximum number of 10,000 iterations was fixed and the stopping criterion defined by Eq. (19) was set as $\varepsilon = 5 \times 10^{-7}$.

4.1. Images reconstruction with ideal data

Fig. 2 presents the tomograms reconstructed using the GIA from the ideal synthetic data. The 2D FEM sensor model was used to reconstruct the images. Table 3 compares the number of iterations, the norm of voltages residual ($||R_k||_2^2$), the correlation coefficient (R^2) and the error on the bulk concentration of the non-conductive phase (e_b) given by

$$e_b = \tilde{C}_b - C_b, \tag{24}$$

where C_b is the bulk concentration of the non-conductive phase and $\tilde{C}_b$ is the bulk concentration computed by

$$\tilde{C}_b = \frac{\sum_{i=1}^{n} C_i A_i}{A_T}, \tag{25}$$

where C_i is the concentration of the non-conductive phase in the area A_i of the ith pixel of image.

These results show that the Landweber and Tikhonov iterations yield very similar results and their respective reconstructed images look very close to the image of reference. The numerical values reported in Table 3 indicate that the Tikhonov iteration with $\lambda = 0.1$ reaches a slightly smaller norm of residuals and a higher R^2 coefficients than with $\lambda = 1$ or the Landweber iteration. In general, both the Landweber and Tikhonov iterations generate good approximations of the images and CPU times remain reasonable: ∼500 iterations/min with Matlab scripts (Version 6.1 Release 12.1) on a Pentium M laptop computer running at 1.80 GHz with 1 Gb of RAM.

4.1.1. Influence of forward operator and recalculation of sensitivity matrix

Fig. 3 and Table 4, respectively, present the reconstructed images and the numerical values obtained with case A using the linear forward projection F_S as the forward operator combined to the same numerical parameters (η, λ, ε) used to generate results in Fig. 2. Results show that the linear forward projection provides a quick approximation in a reduced number of iterations yielding the image in less than 1 s. Looking at values of Tables 3 and 4, it is clear that the results are much less accurate with this linear forward operator, leading to significant errors on the bulk concentration and lower correlation coefficients.

The influence of the linear forward operator on the quality of the results is presented on Fig. 4 where the voltages error (i) and the images error (ii) are presented as a function of the iterations. This example illustrates the poor convergence properties of the Landweber iterations when the linear forward projection is used in the residual calculation of GIA. After a certain number of iterations, the norm of the image error begins to increase while the norm of the residual continues to decrease. Note that the same behaviour was experimented with Tikhonov iterations and similar observations were also reported in the literature [7]. This indicates that the linear forward projection exhibits undesired semi-convergence properties. To avoid the divergence of the algorithm, the iterative process must hence be stopped after a given number of iterations. In practice, the most appropriate number of iterations is very difficult to determine. After comparison of Tables 3 and 4 or from Fig. 4, it is clear that only the F_{FEM} forward operator can ensure the convergence of GIA. Consequently, only the FEM sensor model should be used to compute the residual in GIA when quantitative images are desired, at the price of longer CPU times for post-processing the ERT measurements.

Fig. 4 also compares the norm of the image error along the iterations with the sensitivity matrix recalculated each iteration ($S_k = S(\hat{G}_k)$) and the sensitivity matrix kept constant ($S_k = S_0$). The convergence rates are similar and, surprisingly, the norm of the image error along the iteration is smaller when matrix S is kept constant. Thus, the recalculation of matrix S does not improve the precision of the GIA and could be kept constant without exerting a strong influence on the final results.

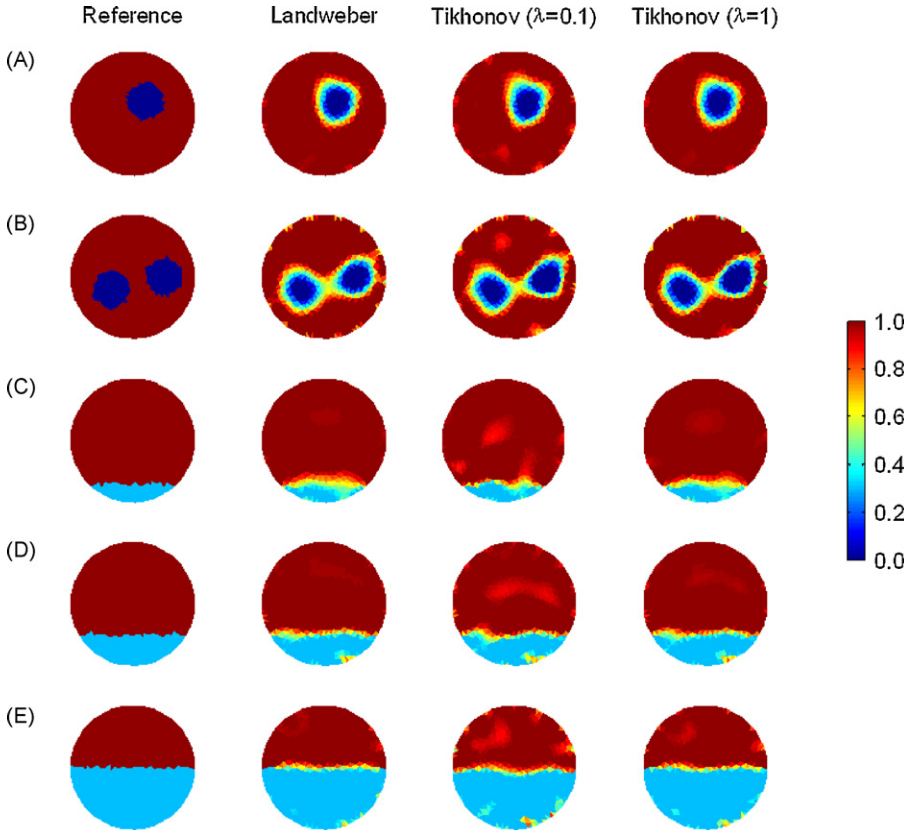

Fig. 5. Reconstructed images with 10% Gaussian noise contamination of ideal synthetic data ($\eta = 0.5$, $\varepsilon = 5 \times 10^{-7}$).

Table 3
Numerical results for images of Fig. 2

Case (C_b)	Algorithm	Number of iterations	R^2 (%)	$\|\|R_k\|\|_2^2$	e_b (%)
A (8.9%)	Landweber	6098	95.6	0.02	−0.1
	Tikhonov (λ = 0.1)	4329	96.3	0.01	−0.1
	Tikhonov (λ = 1)	825	90.3	0.10	0.3
B (17.7%)	Landweber	871	91.7	0.16	−0.5
	Tikhonov (λ = 0.1)	997	93.2	0.06	−0.3
	Tikhonov (λ = 1)	2346	93.2	0.09	−0.4
C (5.6%)	Landweber	286	95.2	0.16	0.3
	Tikhonov (λ = 0.1)	1275	99.0	0.02	0.0
	Tikhonov (λ = 1)	1924	98.0	0.04	0.0
D (11.9%)	Landweber	17	93.4	0.49	1.3
	Tikhonov (λ = 0.1)	3097	99.0	0.03	0.2
	Tikhonov (λ = 1)	4853	98.7	0.03	0.2
E (30.4%)	Landweber	68	97.4	0.56	0.0
	Tikhonov (λ = 0.1)	2987	99.5	0.05	0.0
	Tikhonov (λ = 1)	3985	99.1	0.07	0.0

Table 4
Numerical results for images of Fig. 3

Algorithm	Number of iterations	R^2 (%)	$\|\|R_k\|\|_2^2$	e_b (%)
Landweber	8	73.8	0.88	9.2
Tikhonov (λ = 0.1)	31	67.2	0.74	9.6
Tikhonov (λ = 1)	73	64.6	0.69	10.5

4.1.2. Influence of the relaxation parameter

According to the results of Fig. 2 and Table 3, the calculation of the pseudo-optimal relaxation parameter τ^* (Eq. (21)) allows convergence of the GIA with each case tested. Because the calculation of τ^* requires additional FEM forward solution each iteration ($\tau_k = \tau^*$), a constant value of τ can effectively reduce the CPU time. The selection of an appropriate constant value of τ depends on the image to be reconstructed and there is a minimum critical value of τ for which the GIA convergence is stable and ensures a unique solution. Thus, small enough τ value is required to facilitate the convergence of non-linear inverse problem obviously at the expense of a larger number of iterations.

After a reasonable number of numerical experiments, it was observed that the number of iterations required to reach convergence of the GIA (using both the Landweber and Tikhonov iterations) is inversely proportional to the τ value. For all the cases tested, the same minimum of residuals and the same images were obtained for any value of τ below the critical value. Therefore, if the relaxation parameter is small enough, the GIA converge towards a unique solution and only the number of iterations and CPU times are affected. This observation indicates that by using small constant value or the pseudo-optimal relaxation parameter and allowing large number of iterations, the image reconstructed with the Landweber and Tikhonov methods does not depend on the choice of the relaxation parameter and the number of iteration.

4.2. Image reconstruction with noisy data

So far, the synthetic images have been reconstructed using noise-free data to assess the performance of GIA with ideal data. On the other hand, experimental data are inevitably contaminated by noise and image reconstruction techniques must be robust enough to handle the presence of noise. The noise level influence was studied by contaminating the simulated voltages with a Gaussian normalised distribution (white noise) using

$$\tilde{U} = U(1 + N(0, \delta)), \tag{26}$$

where $\tilde{U}$ is the contaminated voltage vector, δ is the noise level percentage and N is a Gaussian distribution.

Reconstructed images and numerical results for a noise level of $\delta = 10\%$ are reported in Fig. 5 and Table 5 for the case of Landweber and Tikhonov iterations. In these images, under-relaxation of pseudo-optimal parameter with $\eta = 0.5$ was used to ensure convergence of every case tested. With noisy data, the norm of the voltages residual and the error on the bulk concentration of the non-conductive phase increase as expected, while the correlation coefficient decreases slightly. With the Tikhonov iterations, the use of $\lambda = 1$ produces fewer artefacts and higher correlation coefficient than $\lambda = 0.1$.

The results indicate that there is a relatively weak influence of noise level on the quality of reconstructed images when the GIA is used with an adequate parameter values. This suggests that the Landweber and Tikhonov iterations are relatively robust to noisy data, at the expense of lower precision in the reconstructed images as for every tomography technique.

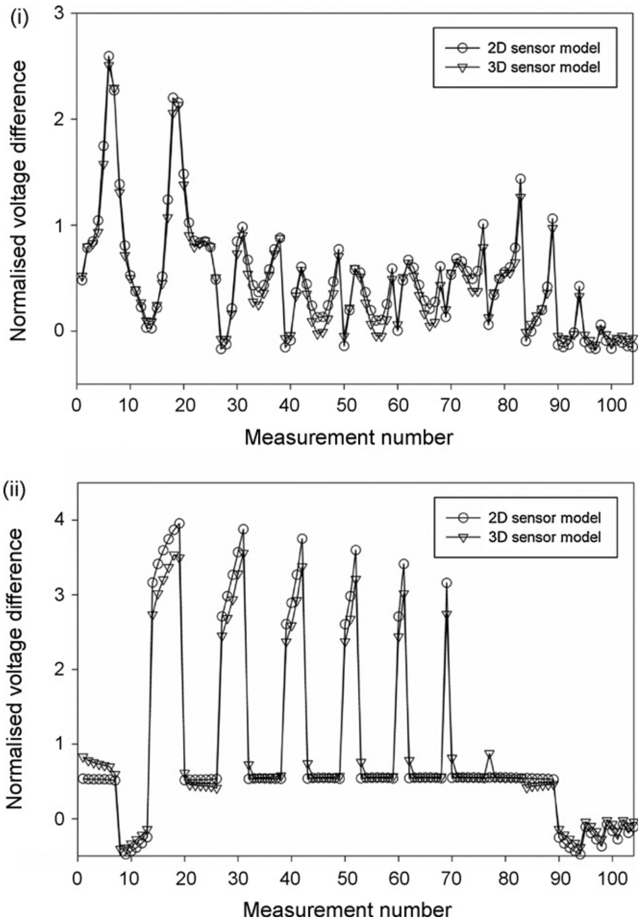

Fig. 6. Normalised voltage differences simulated using 2D and 3D FEM sensor models. (i) Case B and (ii) case E.

4.3. Image reconstruction with non-ideal data

Up to this point, the reconstructed images were based on ideal synthetic data. The same 2D FEM sensor model was used to generate the normalised potential difference data and to compute the residual in the GIA. This means that FEM sensor model can reach a zero residual value if the true image is given. In practice, discrepancies between numerical and experimental sensors are inevitable and a non-ideal sensor has been considered to generate synthetic data using a complete 3D FEM sensor model.

In Fig. 6, non-ideal data generated for the 3D mesh sensor model presented in Fig. 1ii with a contact impedance value of $z = 0.2$ are compared to ideal data. The normalised potential difference vectors are relatively similar for the 2D and the 3D model. Thus, a simple 2D approximation to solve the forward problem of ERT can be used instead of an expensive 3D model. The use of a 2D model is then justified to solve the forward problem in the GIA. However, differences between predictions from 2D or 3D model are not negligible and can potentially limit the performance of image reconstruction algorithms.

Table 5
Numerical results for reconstructed images of Fig. 5

Case (C_b)	Algorithm	Number of iterations	R^2 (%)	$\|\|R_k\|\|_2^2$	e_b (%)
A (8.9%)	Landweber	1555	91.5	0.42	−0.1
	Tikhonov (λ = 0.1)	200	89.9	0.43	0.3
	Tikhonov (λ = 1)	2009	91.0	0.42	0.0
B (17.7%)	Landweber	583	87.9	0.71	−0.2
	Tikhonov (λ = 0.1)	113	86.8	0.73	0.1
	Tikhonov (λ = 1)	1223	87.2	0.69	−0.5
C (5.6%)	Landweber	249	93.0	0.34	0.5
	Tikhonov (λ = 0.1)	88	93.6	0.31	0.5
	Tikhonov (λ = 1)	114	94.0	0.29	0.4
D (11.9%)	Landweber	332	95.9	0.75	0.5
	Tikhonov (λ = 0.1)	143	95.5	0.92	0.5
	Tikhonov (λ = 1)	315	95.8	0.75	0.5
E (30.4%)	Landweber	379	98.2	1.65	−0.1
	Tikhonov (λ = 0.1)	318	94.5	2.55	−1.6
	Tikhonov (λ = 1)	299	97.9	1.71	−0.4

Fig. 7 and Table 6 present the results for images reconstructed from the non-ideal data with the 2D forward model in the GIA. Qualitatively, these images are quite similar to those obtained previously but images reconstructed using non-ideal data are more contaminated by artefacts. Quantitatively, larger residual values were generally obtained leading to lower number of iterations necessary to reach convergence. In spite of that, correlation coefficients and bulk concentration are reasonably similar to those computed from ideal data, meaning that GIA is relatively robust to the presence of non-ideal data. Therefore, a 2D model to solve the forward problem is suitable in the GIA.

5. Images from experimental measurements

ERT measurements were then carried out under laboratory conditions using the *p2000* (ITS, UK) and the pipe sensor described earlier for the synthetic study. Experimental measurements of static conductivity distributions were used to

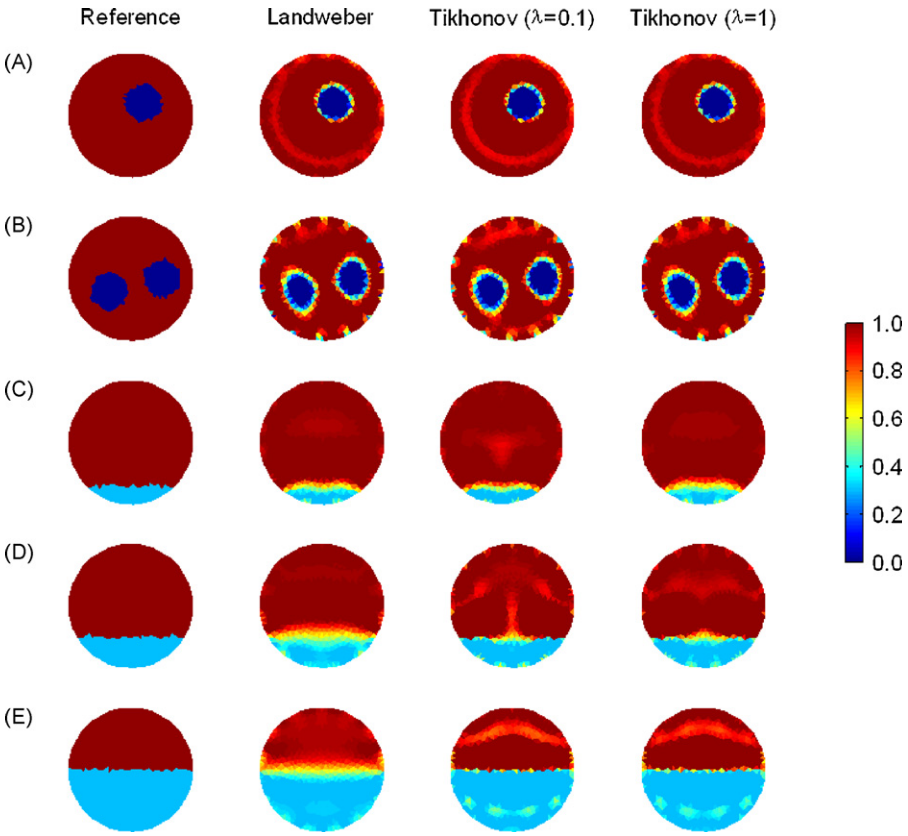

Fig. 7. Reconstructed images with non-ideal synthetic data from 3D sensor model ($\eta = 0.5$, $\varepsilon = 5 \times 10^{-7}$).

reconstruct images using the GIA and were compared to images reconstructed by means of the LBP method implemented in the ITS software.

5.1. *Non-conductive rods*

First, non-conductive rods were inserted in the pipe sensor filled with NaCl solution (325 μS/cm) and ERT measurements were carried out using current injection of 15 mA at frequency of 9.6 kHz. This value of electrical current ensures good signal-to-noise ratio for the reference measurements when having homogenous NaCl solution with electrical conductivity between 300 and 400 μS/cm.

Three test cases of real rods were experimented: centered and off-centered single rod (cases A and B) and two rods (case C). Images reconstructed from these test cases with ITS software and GIA are compared in Fig. 8 and numerical results are reported in Table 7. The LBP method provides good qualitative images of single rod, but cannot distinguish the presence of two rods. Interface of rods are diffuse and minimum conductivity value of images is far from the non-conductive value expected. On the other side, the use of GIA with Landweber and Tikhonov iterations can improve the reconstructed images significantly. The interface of the rods is much sharper and the minimum conductivity values of the tomogram are close to the zero value expected for the non-conductive rods.

As for the synthetic data case study, minor differences were observed between Landweber and Tikhonov results. The Tikhonov iteration seems to produce more artefacts while for the Landweber iteration, the use of pseudo-relaxation parameter cannot ensure convergence of GIA and an under-relaxation procedure with $\eta = 0.5$ is needed to converge properly the single and two rods cases.

5.2. *Bed of solid particles*

Cases of static particle bed at the bottom of the pipe sensor were generated to assess the performance of ERT to quantify the size of a bed of particles in a pipe. For that purpose, the pipe sensor was filled with conductive water and a known amount of solid particles, consisting of spherical glass particles of 100 μm in diameter. The reference measurements were taken with the sensor in vertical position and all the solid particles at bottom of sensor while the measurements with the particle bed were taken with the sensor in a horizontal position.

In a first attempt, ERT measurements were taken for the case of a bed with a bulk concentration of 17 % (v/v) in solid particles, with NaCl solution of around 400 μS/cm and current injection of 15 mA. Images reconstructed for these measurements with LBP method and GIA are presented in Fig. 9a and numerical results are reported in Table 8. At first glance, it seems that the LBP method provides relatively good representation of the bed while GIA produces poor images, which are highly contaminated by artefacts.

It was found that for the case of particle bed, the injection of 15 mA was inappropriate for a conductive solution of 400 μS/cm. In fact, the presence of non-conductive particles increases the electrical resistance of materials in the sensor and relatively high voltages have to be measured by the ERT hardware. Thus, for too high current injection or too small absolute conductivity of mixture, the corresponding voltages to measure can fall out of range of the hardware capability, producing erroneous measurements.

Images were reconstructed using ERT measurement carried out for a bed of solid particles having conductive solution of 1800 μS/cm with 15 mA (Fig. 9b) and 400 μS/cm with 1 mA (Fig. 9c). With these combinations of absolute electrical conductivity and current injection, images reconstructed with GIA provide acceptable approximations of the bed of solid particles and also a reasonable prediction of the solids bulk concentration. For these measurements, the results from the LBP method are qualitatively good, but over-estimate the concentration of solid particles.

The influence of electrical conductivity and current injection on ERT results is also evident by looking at the measurements used to compute images of Fig. 9 and comparing with syn-

Table 6
Numerical results for reconstructed images of Fig. 7

Case (C_b)	Algorithm	Number of iterations	R^2 (%)	$\|\|R_k\|\|_2^2$	e_b (%)
A (8.9%)	Landweber	6347	95.1	0.12	0.0
	Tikhonov (λ = 0.1)	1712	95.3	0.14	0.2
	Tikhonov (λ = 1)	7604	95.1	0.12	0.0
B (17.7%)	Landweber	1021	85.9	0.31	−0.9
	Tikhonov (λ = 0.1)	463	87.8	0.35	−0.4
	Tikhonov (λ = 1)	1248	85.8	0.31	−0.8
C (5.6%)	Landweber	564	93.7	0.13	−0.2
	Tikhonov (λ = 0.1)	108	93.6	0.11	0.0
	Tikhonov (λ = 1)	125	93.0	0.22	0.0
D (11.9%)	Landweber	32	93.9	0.50	0.6
	Tikhonov (λ = 0.1)	2458	95.9	0.16	0.0
	Tikhonov (λ = 1)	4312	96.7	0.14	−0.2
E (30.4%)	Landweber	52	96.0	0.62	0.4
	Tikhonov (λ = 0.1)	1104	97.5	0.26	0.2
	Tikhonov (λ = 1)	6797	98.1	0.21	0.2

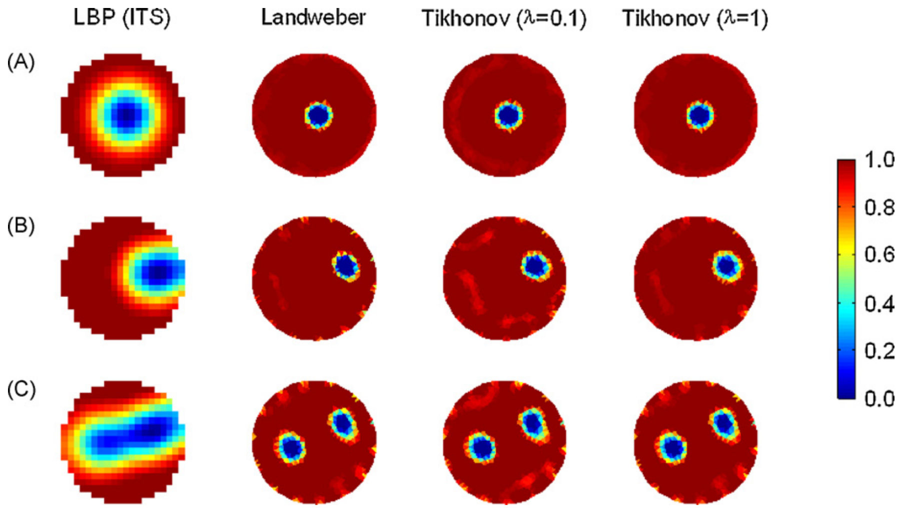

Fig. 8. Reconstructed images of non-conductive rods inserted in the ERT pipe sensor ($\eta = 0.5$, $\varepsilon = 5 \times 10^{-7}$).

Table 7
Numerical results for images of Fig. 8

Case (C_b)	Algorithm	Number of iterations	$\|\|R_k\|\|_2^2$	e_b (%)
Centered rod (4.0%)	ITS LBP	1	–	1.0
	Landweber	7,156	0.09	0.0
	Tikhonov (λ = 0.1)	481	0.10	0.2
	Tikhonov (λ = 1)	10,000	0.09	0.0
Off-centered rod (4.0%)	ITS LBP	1	–	2.0
	Landweber	3,421	0.18	−0.2
	Tikhonov (λ = 0.1)	321	0.22	0.2
	Tikhonov (λ = 1)	3,449	0.19	0.0
2 rods (8.0%)	ITS LBP	1	–	4.1
	Landweber	2154	0.26	−0.2
	Tikhonov (λ = 0.1)	217	0.30	0.3
	Tikhonov (λ = 1)	6301	0.26	−0.1

thetic data generated by 2D FEM sensor model used in GIA (Fig. 10). Results clearly demonstrate that for the combination of 400 μS/cm and 15 mA, the normalised potential differences measured by the hardware are too small and there are important differences with the numerical sensor model predictions. These erroneous measurements of voltage differences explained why GIA failed and cannot reconstruct acceptable images in Fig. 9a.

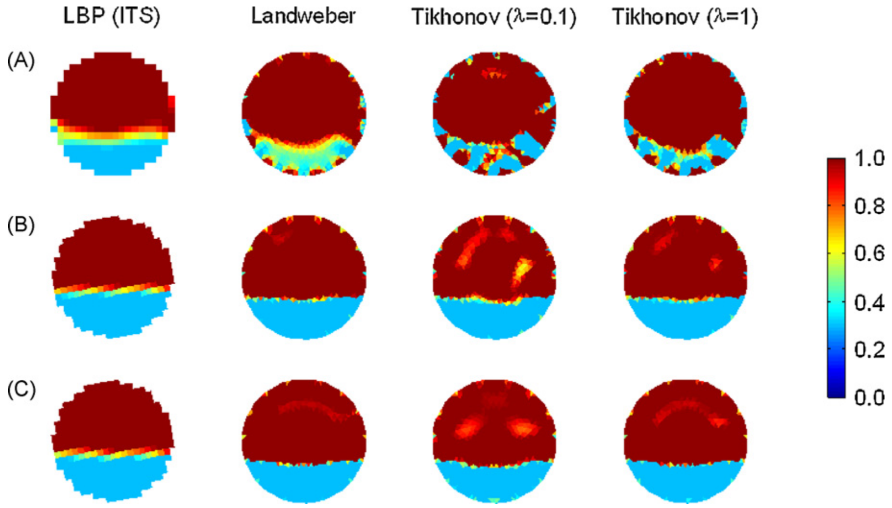

Fig. 9. Reconstructed images of solid particle bed ($C_b = 17.4\%$) at bottom of ERT pipe sensor ($\eta = 0.5$, $\varepsilon = 5 \times 10^{-7}$).

Table 8
Numerical results for reconstructed images of Fig. 9

Case	Algorithm	Number of iterations	$\|\|R_k\|\|_2^2$	e_b (%)
A	ITS LBP	1	–	−0.3
	Landweber	54	2.34	−7.4
	Tikhonov (λ = 0.1)	340	2.40	−6.4
	Tikhonov (λ = 1)	503	2.24	−7.4
B	ITS LBP	1	–	4.6
	Landweber	722	1.04	0.6
	Tikhonov (λ = 0.1)	399	1.16	1.3
	Tikhonov (λ = 1)	775	1.04	0.7
C	ITS LBP	1	–	4.5
	Landweber	1359	1.51	0.1
	Tikhonov (λ = 0.1)	181	1.62	0.2
	Tikhonov (λ = 1)	1652	1.52	0.1

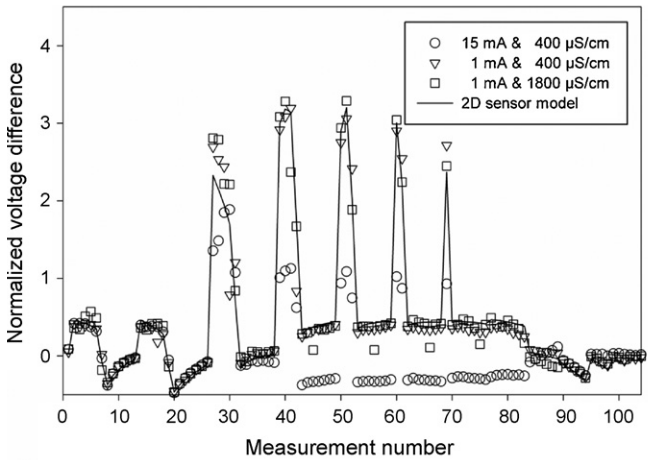

Fig. 10. Comparison of measured and simulated normalised voltage differences of Fig. 9.

5.2.1. Calibration curve

Finally, ERT measurements were obtained for different size of solid particle beds with current injection of 1 mA and electrical conductivity of NaCl solution between 300 and 400 μS/cm. For each measurement, images were reconstructed using LBP and GIA algorithms. The corresponding bulk concentrations (C_b) of solid particles are compared in Fig. 11. These calibration curves show that the use of GIA iterations provides an estimation of C_b with less than 1% (v/v) of error. Using LBP algorithm, C_b was found correct only for small bed of particles (2.5%, v/v), while an over-estimation of about 5% (v/v) is obtained when more particles are present. This is in agreement with calibration results of [17] by the LBP method, where over-estimation was reported. Also, it is interesting to underline that the LBP method in combination with a calibration curve can be suitable to rapidly determine the size of a bed without expensive post-treatment.

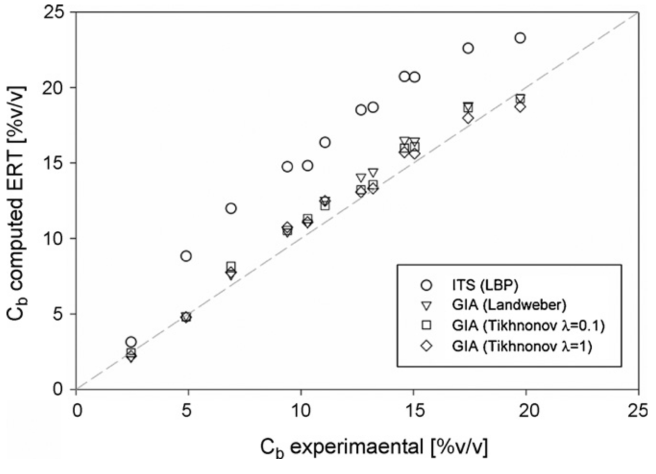

Fig. 11. Calibration data of solid particle bed concentration (C_b) using ERT.

These results show that the GIA can output quantitative images to visualize solid particle beds. The GIA is limited by the quality of experimental measurements. In particular, careful attention must be paid to the choice of current injection intensity according to the absolute conductivity of the sensing materials. This also points out the importance of having numerical model of ERT sensor that efficiently emulates the real sensor data and vice-versa. The FEM sensor models used in this work has shown good capability to simulate sensor data, allowing the diagnostics of the quality of experimental data and determining an appropriate value of current injected.

6. Conclusion

In this paper, quantitative image reconstruction techniques for ERT have been implemented and systematically evaluated using synthetic and experimental test cases. For that purpose, image reconstruction techniques from literature were expressed in a general iterative algorithm, called the GIA, which facilitates their implementation and their comparison.

Synthetic and experimental case studies were used to determine a suitable strategy for the GIA. This consists of the Landweber or Tikhonov iterations, with calculation of voltage residual by a FEM sensor model and calculation of the pseudo-optimal relaxation parameters at each iteration. It was shown that this strategy can ensure convergence and provide a successful quantitative approximation for all test cases tested in this work, without specifying any parameters by a trial and error method. When comparing with direct LBP method, the use of the GIA improved significantly the image precision, allowing for a better interpretation of the ERT measurements.

This work shows that quantitative imaging can be performed with ERT measurements. In this context, ERT coupled with GIA implementation is a promising technique to visualize quantitatively multiphase flow in process application, like monitoring slurry flow in pipe.

Acknowledgments

The financial contribution of NSERC and Total Petrochemicals is gratefully acknowledged. Thanks are also directed to ITS for their technical assistance.

References

[1] H.S. Tapp, E.K. Kemsley, R.H. Wilson, A.J. Peyton, Chemical engineering applications of electrical process tomography, Sens. Actuators B 92 (2003) 17–24.

[2] T. Dyakowski, L.F.C. Jeanmeure, A.J. Jaworski, Applications of electrical tomography for gas–solids and liquid–solids flows—a review, Powder Technol. 112 (2000) 174–192.

[3] M. Wang, Impedance mapping of particulate multiphase flows, J. Flow Meas. Instum. 16 (2005) 183–189.

[4] A.J. Wilkinson, E.W. Randall, T.M. Long, A. Collins, The design of an ERT system for 3D data acquisition and a quantitative evaluation of its performance, Meas. Sci. Technol. 17 (2006) 2088–2096.

[5] E. Fransolet, M. Crine, G. L'Homme, D. Toye, P. Marchot, Electrical resistance tomography sensor simulations: comparison with experiments, Meas. Sci. Technol. 13 (2002) 1239–1247.

[6] N. Polydorides, PhD thesis, Image reconstruction algorithms for soft-field tomography, University of Manchester Institute of science and technology, Manchester, 2002, 250 pp.

[7] W.Q. Yang, L. Peng, Image reconstruction algorithms for electrical capacitance tomography, Meas. Sci. Technol. 14 (2003) 1–13.

[8] B. Su, Y. Zhang, L. Peng, D. Yao, B. Zhang, Use of simultaneous iterative reconstruction technique for electrical capacitance tomography, Chem. Eng. J. 77 (2000) 37–41.

[9] J. Zhao, W. Fu, T. Li, S. Wang, An image reconstruction algorithm based on a revised regularization method for electrical capacitance tomography, Meas. Sci. Technol. 13 (2002) 638–640.

[10] G. Lu, L. Peng, B. Zhang, Y. Liao, Preconditioned Landweber iteration algorithm for electrical capacitance tomography, J. Flow Meas. Instum. 16 (2005) 163–167.

[11] C. Tibirna, D. Edouard, A. Fortin, F. Larachi, Usability of ECT for quantitative and qualitative characterization of trickle-bed flow dynamics subject to filtration conditions, Chem. Eng. Process. 45 (2006) 538–545.

[12] C.J. Grootveld, A. Segal, B. Scarlett, Regularized modified Newton–Raphson technique applied to electrical impedance tomography, Int. J. Imag. Syst. Technol. 9 (1998) 60–65.

[13] M. Wang, Inverse solutions for electrical impedance tomography based on conjugate gradients methods, Meas. Sci. Technol. 13 (2002) 101–117.

[14] O. Isaksen, Review of reconstruction techniques for capacitance tomography, Meas. Sci. Technol. 7 (1996) 325–337.

[15] S. Liu, L. Fu, W.Q. Yang, Optimization of an iterative image reconstruction algorithm for electrical capacitance tomography, Meas. Sci. Technol. 10 (1999) 37–39.

[16] S. Liu, L. Fu, W.Q. Yang, H.G. Wang, F. Jiang, Prior-online iteration for image reconstruction with electrical capacitance tomography, IEE Proc. Sci. Meas. Technol. 151 (2004) 195–200.

[17] Y.S. Fangary, R.A. Williams, W.A. Neil, J. Bond, I. Faulks, Application of electrical resistance tomography to detect deposition in hydraulic conveying systems, Powder Technol. 95 (1998) 61–66.

[18] R. Stevenson, S.T.L. Harrison, N. Miles, J.J. Cilliers, Examination of swirling flow using electrical resistance tomography, Powder Technol. 162 (2006) 157–165.

[19] Y. Dai, A.D. Pachowko, M. Wang, The control of polymer addition to raw waste sludge using electrical resistance tomography—a preliminary study, Part. Part. Syst. Charact. 21 (2004) 228–233.

[20] J.T. Norman, R.T. Bonnecaze, Measurement of solids distribution in suspension flows using electrical resistance tomography, Can. J. Chem. Eng. 83 (2005) 24–36.

[21] L. Pullum, L. Graham, M. Rudman, R. Hamilton, High concentration suspension pumping, Miner. Eng. 19 (2006) 471–477.

[22] F. Dong, Y.B. Xu, L.J. Xu, L. Hua, X.T. Qiao, Application of dual-plane ERT system and cross-correlation technique to measure gas-liquid flows in vertical upward pipe, J. Flow Meas. Instum. 16 (2005) 191–197.

[23] F. Dong, Y. Xu, L. Hua, H. Wang, Two methods for measurement of gas–liquid flows in vertical upward pipe using dual-plane ERT system, IEE Trans. Instrum. Meas. 55 (2006) 1576–1586.

[24] M. Wang, G. Lucas, Y. Dai, N. Panayotopoulos, R.A. Williams, Visualisation of bubbly velocity distribution in a swirling flow using electrical resistance tomography, Part. Part. Syst. Charact. 23 (2006) 321–329.

[25] M. Henningsson, K. Ostergren, P. Dejmek, Plug flow of yoghurt in piping as determined by cross-correlated dual-plane electrical resistance tomography, J. Food Eng. 76 (2006) 163–168.

[26] M. Henningsson, M. Regner, K. Ostergren, C. Tragardh, P. Dejmek, CFD simulation and ERT visualization of the displacement of yoghurt by water on industrial scale, J. Food Eng. 80 (2007) 166–175.

[27] F. Ricard, C. Brechtelsbauer, Y. Xu, C. Lawrence, D. Thompson, Development of an electrical resistance tomography reactor for pharmaceutical processes, Can. J. Chem. Eng. 83 (2005) 11–18.

[28] S. Kim, A.N. Nkaya, T. Dyakowski, Measurement of mixing of two miscible liquids in a stirred vessel with electrical resistance tomography, Int. Commun. Heat Mass Transfer 33 (2006) 1088–1095.

[29] S.J. Stanley, R. Mann, K. Primrose, Interrogation of a precipitation reaction by electrical resistance tomography (ERT), AICHE J. 51 (2005) 607–614.

[30] G.T. Bolton, C.W. Hooper, R. Mann, E.H. Stitt, Flow distribution and velocity measurement in a radial flow fixed bed reactor using electrical resistance tomography, Chem. Eng. Sci. 59 (2004) 1989–1997.

[31] M. Vijayan, H.I. Schlaberg, M. Wang, Effects of Sparger geometry on the mechanism of flow pattern transition in a bubble column, Chem. Eng. J. 130 (2007) 171–178.

[32] H. Jin, M. Wang, R.A. Williams, Analysis of bubble behaviors in bubble columns using electrical resistance tomography, Chem. Eng. J. 130 (2007) 179–185.

[33] E. Fransolet, M. Crine, G. L'Homme, D. Toye, P. Marchot, Analysis of electrical resistance tomography measurements obtained on a bubble column, Meas. Sci. Technol. 12 (2001) 1055–1060.

[34] E. Fransolet, M. Crine, P. Marchot, D. Toye, Analysis of gas holdup in bubble columns with non-Newtonian fluid using electrical resistance tomography and dynamic gas disengagement technique, Chem. Eng. Sci. 60 (2005) 6118–6123.

[35] D. Toye, E. Fransolet, D. Simon, M. Crine, G. L'Homme, P. Marchot, Possibilities and limits of application of electrical resistance tomography in hydrodynamics of bubble columns, Can. J. Chem. Eng. 83 (2005) 4–10.